Available online at www.sciencedirect.com
ScienceDirect
Journal of Crystal Growth 306 (2007) 166–176
JOURNAL OF CRYSTAL GROWTH
www.elsevier.com/locate/jcrysgro

# An application of proper orthogonal decomposition to the stability analysis of Czochralski melt flows

C.J. Jing[a,*], X.L. Liu[a], S. Lin[a,b], D. Henry[c], H. Ben Hadid[c]

[a]*School of Mechanical Engineering, Southwest Jiaotong University, Chengdu, Sichuan 610031, China*
[b]*Mechanical Department, Guangxi Vocational & Technical Institute of Industry, Nanning 530003, China*
[c]*Laboratoire de Mécanique des Fluides et d'Acoustique, CNRS/Université de Lyon, Ecole Centrale de Lyon/Université Lyon 1/INSA de Lyon, ECL, 36 avenue Guy de Collongue, 69134 Ecully Cedex, France*

Received 25 July 2006; received in revised form 8 March 2007; accepted 29 March 2007
Communicated by T. Hibiya
Available online 20 April 2007

**Abstract**

In Czochralski (Cz) crystal growth, the observed complicated melt flows are caused by different types of instability such as buoyancy-induced instability, Marangoni instability or baroclinic instability. In order to grow single crystals of large size and high quality, it is very important to strictly control these melt flows, and in particular to know which instability is dominant in such flows. Proper orthogonal decomposition (POD) is a powerful method to disclose the basic structures of complicated flows. It was traditionally used to analyze flow structures and, more recently, to construct low-order dynamic models able to reproduce complicated flows. An attempt to apply POD to analyze the flow instabilities was conducted in the case of the oscillatory melt flows occurring in an axisymmetric Cz configuration and caused by both buoyancy-induced and surface tension-induced instabilities. Direct numerical simulation was used to obtain the flow fields driven by both buoyancy and surface tension and also the flow fields driven by one of these forces alone. POD was then employed to extract the basic modes from the flow fields. By comparing the basic modes between these situations, the dominant instability involved in such complicated flows has been revealed. In addition, it was found that the basic modes corresponding to buoyancy-induced instability are global and rotating and those to Marangoni-induced instability are local and traveling. All these indicate that the POD could be a powerful method in instability analysis.


*PACS:* 02.60.Cb; 47.20.−k; 47.20.Bp; 47.20.Dr; 81.10.Fq; 83.60.Wc

*Keywords:* A1. Buoyancy instability; A1. Marangoni instability; A1. Proper orthogonal decomposition; A1. Stability analysis; A2. Czochraski crystal growth

## 1. Introduction

The Czochralski (Cz) method is the most common way of growing single crystals. No objection could be raised to the fact that the quality of single crystals is strongly connected with the melt flows. In the Cz crystal growth, the melt flows are governed by many interacting forces, such as buoyancy, surface tension, Coriolis and centrifugal forces, and are then very complicated. Three-dimensional time-dependent and even chaotic flows are common. Many efforts have been made to reveal the mechanisms at the origin of these complicated melt flows [1–16]. Hurle [1] reviewed the various instabilities, which occur in the melt flows during crystal growth. Buoyancy-induced instability is inevitable on earth. Researches conducted by Jing et al. [2–6] have also revealed that surface-tension-induced thermocapillary instability is also a key factor involved in the formation of such complicated melt flows. These indications of Jing et al. were supported by Miller and Pernell [7,8], Hurle [1], Shigematsu et al. [9] and Morita et al. [10]. Jones [11–14] conducted different experiments in which interesting flow patterns were obtained. He particularly emphasized the importance of the baroclinic instability induced by the Coriolis and centrifugal

*Corresponding author. Tel.: +86 28 87602767; fax: +86 28 87634937.
*E-mail address:* chengjunjing@126.com (C.J. Jing).

0022-0248/$ - see front matter © 2007 Elsevier B.V. All rights reserved.
doi:10.1016/j.jcrysgro.2007.03.042

forces. Enger et al. [15] numerically reproduced the complicated melt flows reported by Jones. Jing et al. [16] further investigated the melt flows in a large-scale crucible and focused on the effects of various operating conditions on the melt flows. He concluded that the baroclinic instability could play a dominant role in a large-scale rotating crucible. In the Cz crystal growth system, other instabilities still exist, but, so far, most studies focused on the global results obtained by taking into account various instabilities, so that we only roughly know that some of them are important in the formation of the melt flow. These studies did not clearly show the contribution of each instability to the formation of the melt flow and the characteristic spatial features of the melt flow induced by each instability. They did not clearly answer how each instability modifies the melt flow, either; for example, what way is taken to modify the melt flow by each instability, the rotating, traveling and other motions of the basic rolls induced by the instability? This paper wants to show that the proper orthogonal decomposition (POD) technique (a powerful method to disclose the basic structures of complicated flows and to construct low-order dynamic models able to reproduce complicated flows [17–21]) can be used to give a better understanding of such melt flows and, in particular, analyze the different instability contributions. As a first stage, a simple axisymmetric Cz melt flow involving buoyancy and thermocapillary forces is chosen to show the potentiality of such an approach.

## 2. Problem description

The geometry considered in this study is depicted in Fig. 1. It corresponds to an axisymmetric Cz model. The radius and height of the crucible are $r_c$ and $h$, respectively, and the radius of the crystal is $r_s$. As first step of application of POD to instability analysis, only buoyancy and thermocapillary instabilities can be triggered in the model. The crucible and the crystal are supposed to be both at rest, which excludes the baroclinic instability. The free surface of the melt and the melt/crystal interface are considered as flat. The temperatures of the melt/crystal interface and the sidewall are taken as the melting point, $T_m$, and a constant value, $T_c$ ($T_c > T_m$),

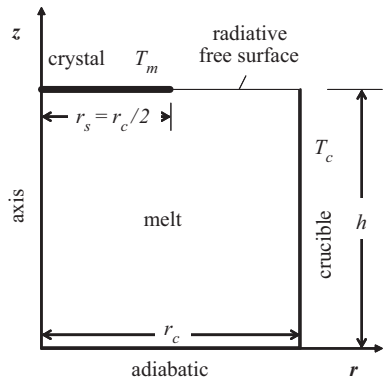


Fig. 1. Axisymmetric Czochralski model.

respectively. The heat loss at the free surface of the melt is assumed to be due only to radiation towards the ambience at temperature $T_a$, whereas the bottom of the crucible is considered as adiabatic. The melt is assumed to be an incompressible Newtonian Boussinesq fluid and the flow is considered as laminar. The no-slip condition is used for all the physical boundaries of the melt except for the free surface, which is considered to be stress free or submitted to thermocapillary effects. For the simplified Cz configuration, the nondimensional mathematical model can be expressed as follows:

$$\frac{V_r}{R}+\frac{\partial V_r}{\partial R}+\frac{\partial V_z}{\partial Z}=0, \tag{1}$$

$$\frac{\partial V_r}{\partial \tau}+V_r\frac{\partial V_r}{\partial R}+V_z\frac{\partial V_r}{\partial Z} =-\frac{\partial P}{\partial R}+\left(-\frac{V_r}{R^2}+\frac{1}{R}\frac{\partial V_r}{\partial R}+\frac{\partial^2 V_r}{\partial R^2}+\frac{\partial^2 V_r}{\partial Z^2}\right), \tag{2}$$

$$\frac{\partial V_z}{\partial \tau}+V_r\frac{\partial V_z}{\partial R}+V_z\frac{\partial V_z}{\partial Z} =-\frac{\partial P}{\partial Z}+\left(\frac{1}{R}\frac{\partial V_z}{\partial R}+\frac{\partial^2 V_z}{\partial R^2}+\frac{\partial^2 V_z}{\partial Z^2}\right)+Gr(T-1), \tag{3}$$

$$\frac{\partial T}{\partial \tau}+V_r\frac{\partial T}{\partial R}+V_z\frac{\partial T}{\partial Z}=\frac{1}{Pr}\left(\frac{1}{R}\frac{\partial T}{\partial R}+\frac{\partial^2 T}{\partial R^2}+\frac{\partial^2 T}{\partial Z^2}\right). \tag{4}$$

The nondimensional parameters involved in the equations are the Grashof number $Gr = g\beta T_m r_c^3/\nu^2$ and the Prandtl number $Pr = \nu/\alpha$, where $g$ is the gravitational acceleration, $\beta$ is the coefficient of volumetric thermal expansion, $\nu$ is the kinematic viscosity and $\alpha$ is the thermal diffusivity.

The boundary conditions are the following:

$$\text{at the melt/crystal interface}: \quad V_r = V_z = 0 \quad \text{and} \quad T = 1, \tag{5}$$

$$\text{at the free surface}: \quad \frac{\partial V_r}{\partial Z} = -Ma\frac{\partial T}{\partial R}, \quad V_z = 0$$
$$\text{and} \quad -\frac{\partial T}{\partial Z} = R_{rad}(T^4 - T_a^4), \tag{6}$$

$$\text{at the sidewall of the crucible}: \quad V_r = V_z = 0$$
$$\text{and} \quad T = T_c/T_m, \tag{7}$$

$$\text{at the bottom of the crucible}: \quad V_r = V_z = 0$$
$$\text{and} \quad \partial T/\partial Z = 0, \tag{8}$$

$$\text{at the axis}: \quad V_r = 0, \ \partial V_z/\partial R = \partial T/\partial R = 0. \tag{9}$$

The nondimensional parameters appearing in the boundary conditions are the Marangoni number $Ma = \gamma_T T_m r_c/\mu\nu$, and a radiation parameter $R_{rad} = \varepsilon\sigma T_m^3 r_c/\lambda$, where $\gamma_T$ is the surface tension/temperature coefficient, $\mu$ is

the dynamic viscosity, $\varepsilon$ is the emissivity, $\sigma$ is the Stefan–Boltzmann constant, and $\lambda$ is the thermal conductivity. In deriving the above equations, the characteristic length $r_c$, velocity $v/r_c$ and temperature $T_m$ were used. Finally, the thermal physical properties of $LiNbO_3$ melt [9] were used in the calculations.

There are many ways to solve the above equations. In this paper, Eqs. (1)–(9) were discretized using the finite-volume method with a staggered arrangement of the variables. Central difference was used for all spatial derivatives and first-order forward difference for the time derivatives. For the convective terms, Kawamura scheme [22] was applied, and HSMAC algorithm was employed to solve the pressure-correction equation. A time step, $\Delta\tau = 10^{-6}$ and a grid of $60 \times 60$ points were tested to be suitable for our study.

Before the presentation of the results, it is necessary to describe the POD.

## 3. POD

POD is a rigorous procedure for extracting a basis of characteristic modes from sampled time evolution signals. These modes are the eigenfunctions of an integral operator based on the spatial correlation function. They are shown to form an orthogonal basis for the function space in which the process resides, and to represent this process in the most efficient way [23]. Directly applying this procedure to a discretized problem involves extremely considerable computing task because the spatial correlation matrix (the eigenvalues of which we want to obtain) is usually very large. A more accessible approach that is referred to as 'the method of snapshots' was proposed by Sirovich [18,19]. This method which invokes the ergodic hypothesis allows to reduce the computation task to a much more tractable eigenproblem with a size $N$ equal to the number of snapshots of the flow field which have been obtained by direct numerical simulation (usually of the order of some hundreds). The method of snapshots is presented in a practical way in the following.

The flow fields $\boldsymbol{V}(\boldsymbol{x},\tau)$ obtained through the $N$ snapshots are decomposed into time-averaged parts $\bar{V}(x)$ and time-varying parts $\boldsymbol{v}'(\boldsymbol{x},\tau)$, i.e.,

$$\boldsymbol{V}(\boldsymbol{x},\tau) = \bar{\boldsymbol{V}}(x) + \boldsymbol{v}'(\boldsymbol{x},\tau). \tag{10}$$

The two time correlation matrix $C_{m,n}$ is then constructed from the velocity samples as

$$C_{m,n} = \frac{1}{N}(\boldsymbol{v}'(\boldsymbol{x},\tau_m), \boldsymbol{v}'(\boldsymbol{x},\tau_n)), \quad m,n = 1,2,\ldots,N, \tag{11}$$

where the outer parentheses $(.,.)$ represent the inner product defined as

$$(\boldsymbol{a},\boldsymbol{b}) = \int_D \boldsymbol{a}(\boldsymbol{x}) \cdot \boldsymbol{b}(\boldsymbol{x})\,\mathrm{d}x, \tag{12}$$

where $\boldsymbol{a}$ and $\boldsymbol{b}$ are two vectors and $D$ is the flow domain.

The eigenvalues $\lambda_i$ associated to the correlation matrix (Eq. (11)) and the corresponding eigenvectors $A_i^m$, $m = 1, N$, can be calculated, which gives

$$C_{m,n}A_i^n = \lambda_i A_i^m. \tag{13}$$

Finally, the characteristic modes (also called empirical eigenfunctions) $\boldsymbol{\Phi}_i(\boldsymbol{x})$ (here normalized) are obtained as linear combinations of the time-varying parts,

$$\boldsymbol{\Phi}_i(\boldsymbol{x}) = \sum_{m=1}^{N} A_i'^m \boldsymbol{v}'(\boldsymbol{x},\tau_m) \tag{14}$$

with $A_i'^m = A_i^m / \sqrt{\lambda_i N \sum_{m=1}^{N} (A_i^m)^2}$.

The eigenvalues and empirical eigenfunctions have the following interesting properties:

(a) The eigenvalues are real, non-negative and can be ordered. Each eigenvalue $\lambda_i$ represents the relative contribution of the corresponding mode $\boldsymbol{\Phi}_i(\boldsymbol{x})$ to the total fluctuation kinetic energy of the flow field.

(b) The eigenfunctions are orthogonal and have been normalized , so that they verify $(\boldsymbol{\Phi}_i\ ,\ \boldsymbol{\Phi}_j\ ) = \delta_{i,j}$ . They are divergence free $(\nabla \cdot \boldsymbol{\Phi}_i = 0)$ since they are constructed as linear combinations of the incompressible flow snapshots $\boldsymbol{v}'\ (\boldsymbol{x}\ ,\ \tau\ )$ .

(c) The eigenfunctions found by POD are shown to be optimal for modeling or reconstructing a flow field compared to all other decompositions. The time-varying parts $\boldsymbol{v}'(\boldsymbol{x},\tau)$ can then be expressed in terms of these normalized eigenfunctions as

$$\boldsymbol{v}'(\boldsymbol{x},\tau) = \sum_{i=1}^{M} a_i(\tau)\boldsymbol{\Phi}_i(\boldsymbol{x}), \tag{15}$$

where $a_i\ (\tau\ )$ are coefficients depending on time, and $M$ is the number of the first most important modes retained in the expansion for velocity. When $M\ = N$ , the original sampled signal can be reproduced exactly, with

$$a_i(\tau) = a_i^m = N\lambda_i A_i'^m. \tag{16}$$

Usually $M$ is much smaller than the number of snapshots, $N$, and is chosen so that the set of eigenfunctions captures most of the fluctuation energy. For example in Sirovich [19], the choice is made by taking $\xi\ > 99\%$, where $\xi \equiv \sum_{i=1}^{M}\lambda_i / \sum_{i=1}^{N}\lambda_i$, meaning that the first $M$ modes capture more than 99% of the fluctuation kinetic energy.

The procedure for extracting the characteristic modes of the temperature field is similar to that for the flow field.

From the above description, it can be understood that POD is a powerful method to extract the basic flow structures from a given flow field. Moreover, POD can give an indication on the contribution of each basic flow structure to the total flow field. It was traditionally used to analyze flow structures [17–19] and, more recently, to construct low-order dynamic models able to reproduce complicated flows [20,21].

In this study, POD was used to analyze the contributions of various instabilities to the flow fields obtained for different values of the parameters.

## 4. Approach of the problem

When a flow field is governed by two or more instabilities, each instability plays a certain role in organizing the flow field. Because of the nonlinearity of the governing equations, the flow field cannot be expressed only by the linear summation of each flow field induced by the corresponding instability, and each contribution of the instabilities to the flow field also cannot be determined in a simple way. When the flow is time dependent, it is still more difficult to clarify the contributions of each instability to the total flow field. However, according to POD, it can be understood that, despite the complexity and time dependence of a flow field, the set of the basic structures composing the flow field can be obtained, and can be also easily compared to the set corresponding to another flow field. Moreover, assuming that the first basic structure obtained by POD corresponds to the dominant instability, the analysis of this structure will reveal a characteristic feature of this instability. Since the eigenvalue associated to the basic structure represents the relative contribution of this structure to the total flow, thus, through POD, it is possible to quantitatively analyze the contribution of the corresponding instability to the flow field.

In this study, a simple model corresponding to an axisymmetric Cz melt flow driven by both buoyancy and surface tension forces, was used. Numerical simulation has the advantage that it is possible to obtain the flow field driven by a single force. For convenience, the flow driven by both buoyancy and surface tension is denoted as the ($Gr$+$Ma$)-driven flow, the flow driven only by buoyancy as the $Gr$-driven flow and the flow driven only by surface tension as the $Ma$-driven flow. By comparing the basic flow structures of the ($Gr$+$Ma$)-driven flow with those of the $Gr$-driven flow and of the $Ma$-driven flow, the nature of the dominant instability in general situations can be revealed.

## 5. Results and discussion

### 5.1. Analysis based on DNS

Numerous DNS calculations were first performed for various sets of ($Gr$, $Ma$). The steady or oscillatory character of the flow states thus obtained is indicated in Table 1. Moreover for some oscillatory cases, precisions on the time evolution and the spatial characteristics of the flow state are given in Figs. 2 and 3. More precisely, Fig. 2 shows the time evolutions of the velocity $V_r$ at a monitoring point ($R = 0.75$, $Z = 0.98$, i.e., a little below the free surface) for some representative sets of ($Gr$, $Ma$). In each graph, the DNS results are depicted as dashed lines. Concerning Fig. 3, it shows instantaneous streamline contours for some representative cases in order to better understand the topology of the DNS flow fields.

Table 1
Flow properties for various sets of $Gr$ and $Ma$

| $Ma$ | $Gr$ | | | | | | |
|---|---|---|---|---|---|---|---|
| | 0 | $2.52\times10^{3}$ | $2.52\times10^{4}$ | $2.52\times10^{5}$ | $2.52\times10^{6}$ | $5.04\times10^{6}$ | $2.52\times10^{7}$ |
| 0 | S | S | S | S | S | O | O |
| $4.94\times10^{1}$ | S | S | S | S | S | O | O |
| $4.94\times10^{2}$ | S | S | S | S | S | O | O |
| $4.94\times10^{3}$ | S | S | S | S | S | S | O |
| $4.94\times10^{4}$ | O | O | O | O | O | O | O |
| $4.94\times10^{5}$ | O | O | O | O | O | O | O |

S indicates a steady flow and O an oscillatory flow.

Analyzing the results more in details, it can be seen that without the Marangoni effect ($Ma = 0$), i.e. when the flow is driven only by buoyancy (see the first row of Table 1), the flow is first steady in a large range of $Gr$ values, but, with the increase of $Gr$, the flow eventually loses its stability and transits to an oscillatory state at a critical value of $Gr$ between $2.52\times10^{6}$ and $5.04\times10^{6}$. Therefore, the oscillatory flows occurring at $Ma = 0$ when $Gr \geqslant 5.04\times10^{6}$ are the result of a buoyancy instability. Some precisions on this limit case at $Gr = 5.04\times10^{6}$ are given by the time evolution shown in Fig. 2a and by the streamline contours given in Figs. 3a and b. These contours are taken at the two instants indicated by dots in Fig. 2a and corresponding to a peak and a valley of the time evolution. It is thus found that the oscillation is regular and corresponds to the displacement of the main flow cell from the top-right of the geometry to the bottom-left. It should be also emphasized that the oscillation is global inside the cavity. A further increase of $Gr$ up to $Gr = 2.52\times10^{7}$ (Figs. 2b and 3c) leads to a flow state for which the time evolution becomes irregular and the flow field more complicated, but the observed oscillation is still global inside the cavity.

On the other hand, in the case without buoyancy ($Gr = 0$), i.e. when the flow is driven only by the Marangoni effect (see the first column of Table 1), the flow is first steady and, with the increase of $Ma$, becomes oscillatory at a critical value of $Ma$ between $4.94\times10^{3}$ and $4.94\times10^{4}$. As a consequence, the oscillatory flows occurring at $Gr = 0$ when $Ma \geqslant 4.94\times10^{4}$ are the result of the Marangoni instability. Some precisions on this limit case at $Ma = 4.94\times10^{4}$ are given in Figs. 2c and 3d. The amplitude and the frequency of the oscillation are large compared to what was obtained at ($Gr = 5.04\times10^{6}$, $Ma = 0$), but the main oscillations are now confined in a thin layer below the free surface whereas the oscillations in the bulk are rather weak. Finally, a same type of behavior is obtained at $Ma = 4.94\times10^{5}$ (see Figs. 2d and 3e), except that the flow velocities are larger and the frequency of the oscillations as well.

However, when the flow is driven by both buoyancy and surface tension forces, it is not easy to point out immediately which one of buoyancy instability and Marangoni instability plays a dominant role in inducing

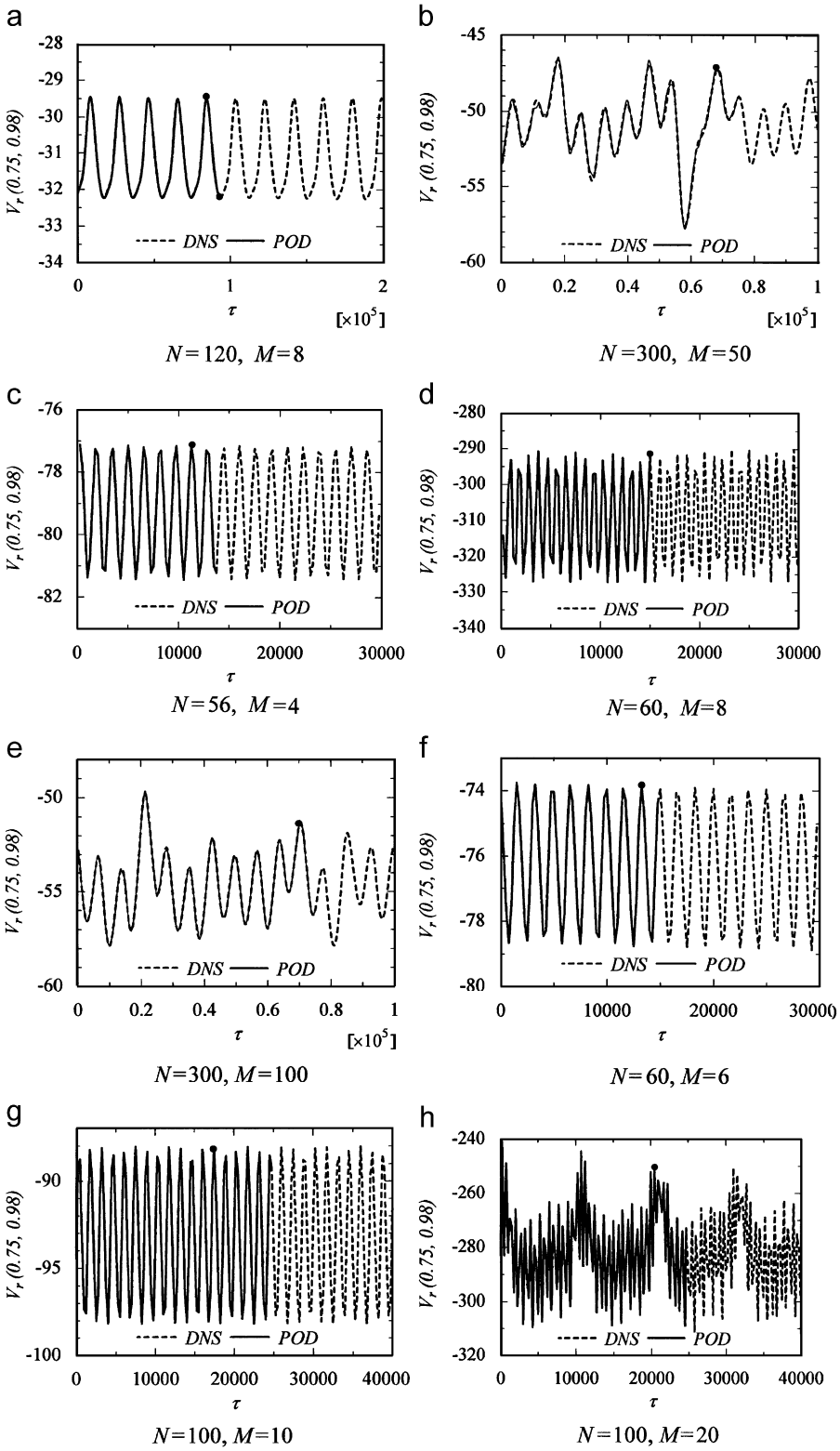


Fig. 2. Time evolutions of the velocity $V_r$ at a monitoring point ($R = 0.75$, $Z = 0.98$, i.e., a little below the free surface) for some representative sets of ($Gr$, $Ma$). The dashed lines correspond to the DNS results, the solid lines to the results reconstructed by POD. $N$ is the number of snapshots used to perform the POD and $M$ is the number of modes used to reconstruct the flow fields, (a) $Gr = 5.04 \times 10^6$, $Ma = 0$; (b) $Gr = 2.52 \times 10^7$, $Ma = 0$; (c) $Gr = 0$, $Ma = 4.94 \times 10^4$; (d) $Gr = 0$, $Ma = 4.94 \times 10^5$; (e) $Gr = 2.52 \times 10^7$, $Ma = 4.94 \times 10^3$; (f) $Gr = 5.04 \times 10^6$, $Ma = 4.94 \times 10^4$; (g) $Gr = 2.52 \times 10^7$, $Ma = 4.94 \times 10^4$; and (h) $Gr = 2.52 \times 10^7$, $Ma = 4.94 \times 10^5$.

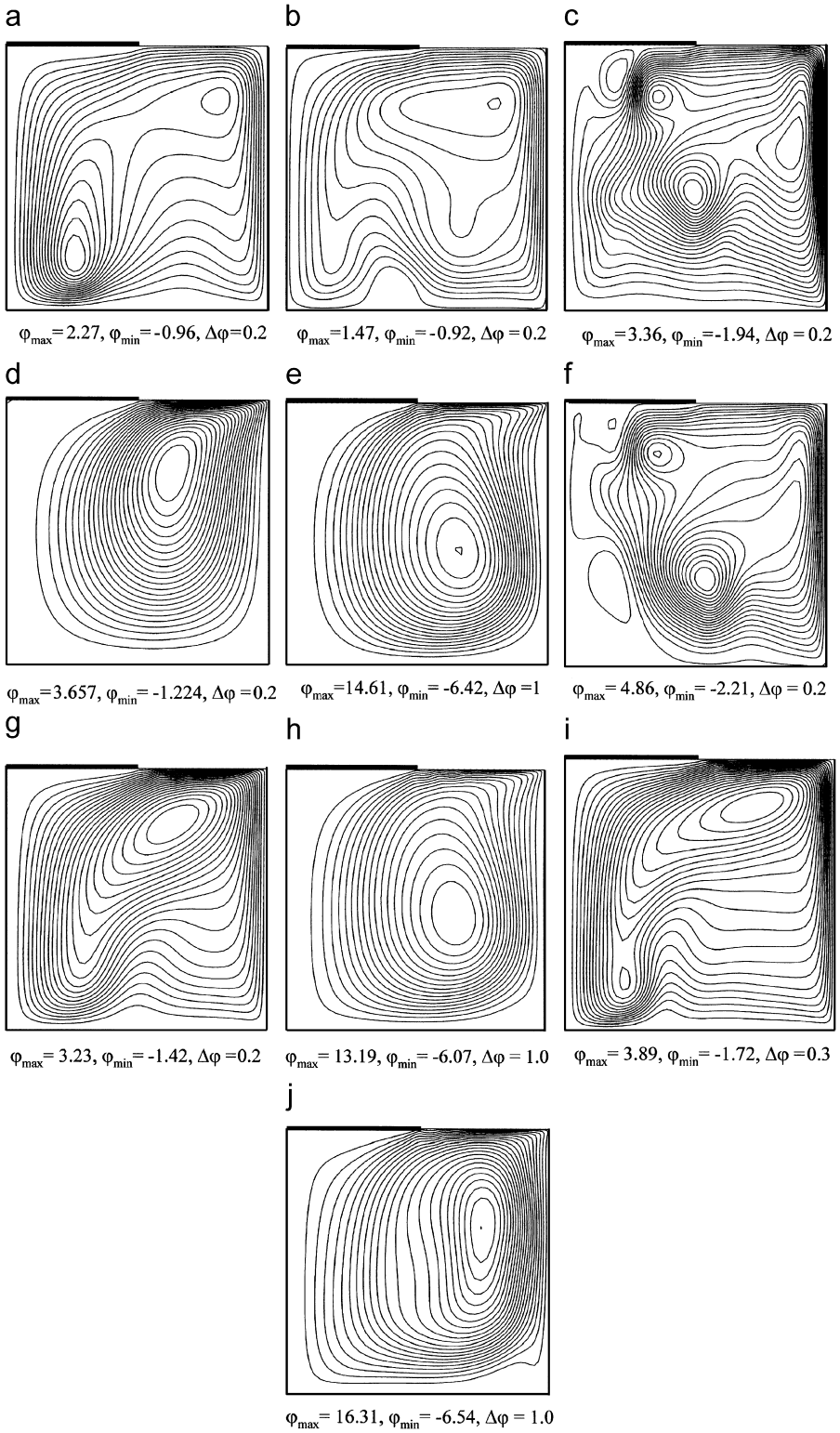


Fig. 3. Instantaneous flow fields expressed through streamfunction contours (streamlines) for various sets of ($Gr$, $Ma$). In this figure as well as in the following figures, the streamfunction is defined as $\partial\varphi/\partial r = -rV_z$, $\partial\varphi/\partial Z = rV_r$. $\varphi_{max}$, $\varphi_{min}$ shown below each figure are the maximum and minimum values of $\varphi$· $\Delta\varphi$ is the interval between the streamfunction contours, (a), (b) $Gr = 5.04 \times 10^6$, $Ma = 0$; (c) $Gr = 2.52 \times 10^7$, $Ma = 0$; (d) $Gr = 0$, $Ma = 4.94 \times 10^4$; (e) $Gr = 0$, $Ma = 4.94 \times 10^5$; (f) $Gr = 2.52 \times 10^7$, $Ma = 4.94 \times 10^3$; (g) $Gr = 5.04 \times 10^6$, $Ma = 4.94 \times 10^4$; (h) $Gr = 5.04 \times 10^6$, $Ma = 4.94 \times 10^5$; (i) $Gr = 2.52 \times 10^7$, $Ma = 4.94 \times 10^4$; and (j) $Gr = 2.52 \times 10^7$, $Ma = 4.94 \times 10^5$.

the oscillatory flow. Let us try to go further in the analysis. First, the steady state at ($Gr = 5.04 \times 10^6$, $Ma = 4.94 \times 10^3$) (see Table 1) can be viewed as the result of the stabilization by the thermocapillary effect at $Ma = 4.94 \times 10^3$ of the buoyancy instability corresponding to $Gr = 5.04 \times 10^6$. This stabilization of the buoyancy-induced circular bulk flow can be connected to the acceleration induced by the thermocapillary effect, which in the present model, acts in the same direction as buoyancy. At $Ma = 4.94 \times 10^3$, the increase of the velocity by the thermocapillary effect is enough to suppress the weak oscillations which appeared in the purely buoyancy-driven case. With the increase of $Gr$ at the same value of $Ma$, the flow becomes oscillatory, as can be seen for ($Gr = 2.52 \times 10^7$, $Ma = 4.94 \times 10^3$) (Figs. 2e and 3f). Therefore, it can be inferred that this oscillatory flow is caused by the buoyancy instability, or more precisely, that the buoyancy instability has a dominant contribution to the oscillatory flow. Similarly, it can be inferred that the Marangoni instability is responsible for the oscillatory flow at ($Gr = 5.04 \times 10^6$, $Ma = 4.94 \times 10^4$) (see Figs. 2f and 3g, as this oscillatory flow is developed from the steady flow at ($Gr = 5.04 \times 10^6$, $Ma = 4.94 \times 10^3$) just by increasing the Marangoni number $Ma$. For this oscillatory flow, as well as for the flow at ($Gr = 5.04 \times 10^6$, $Ma = 4.94 \times 10^5$) (see Fig. 3h, we can say that it is now the Marangoni instability which has a dominant contribution.

For all the flow states just mentioned, the DNS analysis can give a qualitative answer about the dominant instability involved in such ($Gr + Ma$)-driven flows. But, for the oscillatory flows at ($Gr = 2.52 \times 10^7$, $Ma = 4.94 \times 10^4$) (see Figs. 2g and 3i and ($Gr = 2.52 \times 10^7$, $Ma = 4.94 \times 10^5$) (see Figs. 2h and 3j, the DNS analysis cannot directly give any indication. But, the POD approach proposed by the authors in the present paper can give more precise information about the dominant instability.

### 5.2. Analysis based on POD

Following the procedure described in Section 3, POD was applied to various oscillatory solutions obtained by DNS for different sets of ($Gr$, $Ma$). For each case, a set of snapshots (called signal sample) was collected from the fully developed oscillatory flow. In order to exactly capture the flow characteristics, the sample should cover enough periods of oscillation and the time interval between the snapshots should be as short as possible. The time interval between snapshots is $250\Delta\tau$ for all cases except for the case at ($Gr = 5.04 \times 10^6$, $Ma = 0$), for which it is $1000\Delta\tau$. The number of snapshots used to perform the POD, $N$, and the number of the first important basic modes used to reproduce the flow field, $M$, are indicated below each graph in Fig. 2. In this figure, the results reproduced by POD are depicted as solid lines and compared to those obtained by DNS (dashed lines). It can be seen that the solid lines and the dashed lines coincide exactly for all the cases shown, which on one hand proves that the parameters $M$ and $N$ have been well chosen and on the other hand denotes the real potentiality of POD to reproduce oscillatory flows. The number of modes used to reproduce the original flows corresponds in fact to the $M$ first basic modes, which together capture 99.9% of the fluctuating kinetic energy. In the following, we will see how useful and powerful is the POD in investigating the dominant instability in a ($Gr + Ma$)-driven flow.

First, the basic modes for the purely buoyancy-driven oscillatory flow at ($Gr = 5.04 \times 10^6$, $Ma = 0$) and for the purely Marangoni-driven oscillatory flow at ($Gr = 0$, $Ma = 4.94 \times 10^4$) have been extracted using POD and are shown in Figs. 4 and 5, respectively. In fact, only the first two basic modes are presented in these figures through streamline contours with an interval between the contours equal to 0.005. The maximum and minimum values of the streamlines are listed below each figure. The percentage shown in the figures below each mode indicates the corresponding contribution of the mode to the total fluctuation kinetic energy of the flow. From that, it can be stated that for these two cases the first two modes

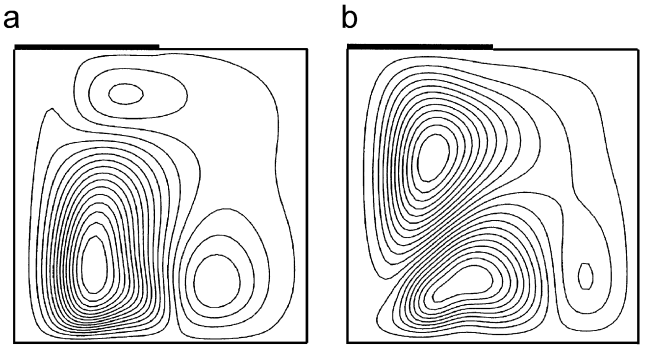


Fig. 4. Streamlines for the first two basic modes obtained by POD from the purely buoyancy-driven oscillatory flow at ($Gr = 5.04 \times 10^6$, $Ma = 0$). In this figure as well as in the following figures, the data given in % indicate the percentage of the fluctuation kinetic energy captured by the corresponding mode, (a) mode 1, 59.3%; and (b) mode 2, 33.6%.

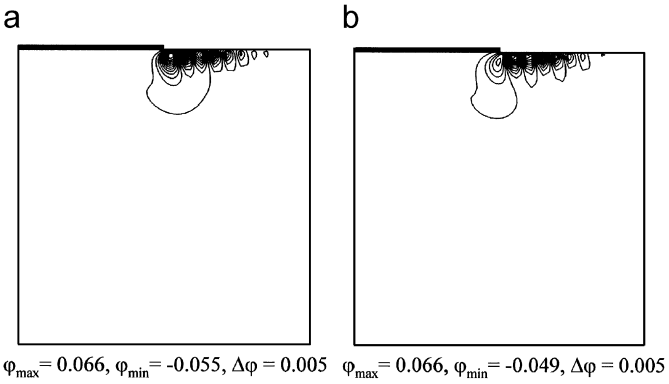


Fig. 5. Streamlines for the first two basic modes obtained by POD from the purely Marangoni-driven oscillatory flow at ($Gr = 0$, $Ma = 4.94 \times 10^4$), (a) mode 1, 52.2%; and (b) mode 2, 47.1%.

together contribute a lot to the fluctuation kinetic energy, more than 92% and 99%, respectively. Figs. 4 and 5 clearly show the differences between the basic modes in the two situations. The basic modes of the oscillatory flow induced by buoyancy are global bulk modes, whereas those of the oscillatory flow induced by surface tension are localized modes, near the free surface. As already mentioned, the basic modes are intrinsic and time independent, and they indicate the origins of the fluctuation field. From these structures of the basic modes, it can be clearly stated that the buoyancy instability occurs globally over the whole fluid bulk and that the Marangoni instability occurs locally near the free surface.

In Fig. 6 are shown the first two basic modes for the oscillatory flow at ($Gr = 5.04 \times 10^6$, $Ma = 4.94 \times 10^4$). These first two modes contribute up to 98% to the total fluctuation kinetic energy. Obviously, the structure of these basic modes is similar to the structure of the modes obtained in the purely Marangoni-driven situation (see Fig. 5). It can be concluded that the oscillatory flow occurring at ($Gr = 5.04 \times 10^6$, $Ma = 4.94 \times 10^4$) is mainly induced by the Marangoni instability. Furthermore, as shown in Fig. 7, the basic structures at ($Gr = 5.04 \times 10^6$, $Ma = 4.94 \times 10^5$) are also similar to those shown in Fig. 5, indicating that the flow is still mainly induced by the Marangoni instability. In this case, the first two modes contribute 98% to the total fluctuation kinetic energy. These conclusions are the same as those obtained by the analysis based on DNS in the previous section. However, these conclusions cannot be obtained easily from the instantaneous DNS flow fields, as those shown in Figs. 3g and h. This already indicates the interest of POD in stability analysis.

Before the cases for a higher $Gr$ number ($Gr = 2.52 \times 10^7$, last column in Table 1) are discussed, the basic structures for the purely buoyancy-driven oscillatory flow at ($Gr = 2.52 \times 10^7$, $Ma = 0$) are shown in Fig. 8. In this case, the streamline contours of the first four basic modes are shown. Unlike the cases discussed before where the first two modes capture most of the fluctuation kinetic energy, the first four modes only capture 65% of the fluctuation kinetic energy and 40 modes are necessary to reach 99%, which indicates that the fluctuation kinetic energy is scattered among the modes. Nevertheless, the characteristic structure of the basic modes is found to be global and to affect the bulk, which again emphasizes this characteristic of the buoyancy instability.

If the Marangoni effect is introduced but remains weak ($Ma \leqslant 4.94 \times 10^3$), the oscillatory flow is still induced by the buoyancy instability, in good agreement with what was

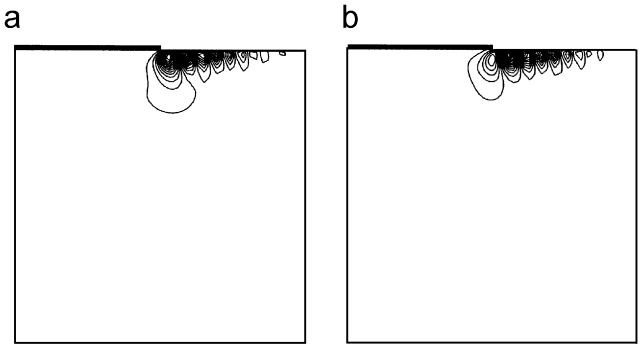


Fig. 6. Streamlines for the first two basic modes obtained by POD from the buoyancy- and Marangoni-driven oscillatory flow at ($Gr = 5.04 \times 10^6$, $Ma = 4.94 \times 10^4$), (a) mode 1, 51.6%; and (b) mode 2, 46.4%.

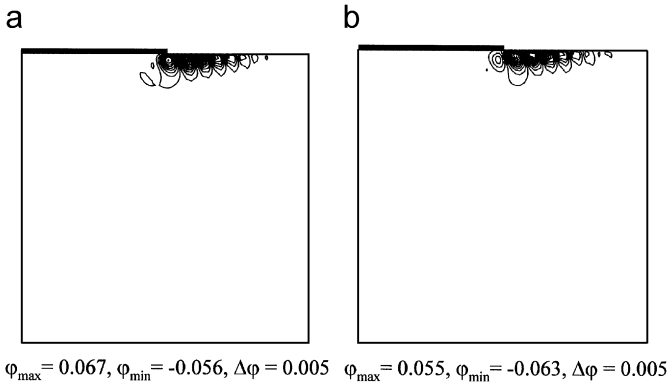


Fig. 7. Streamlines for the first two basic modes obtained by POD from the buoyancy- and Marangoni-driven oscillatory flow at ($Gr = 5.04 \times 10^6$, $Ma = 4.94 \times 10^5$), (a) mode 1, 49.5%; and (b) mode 2, 48.5%.

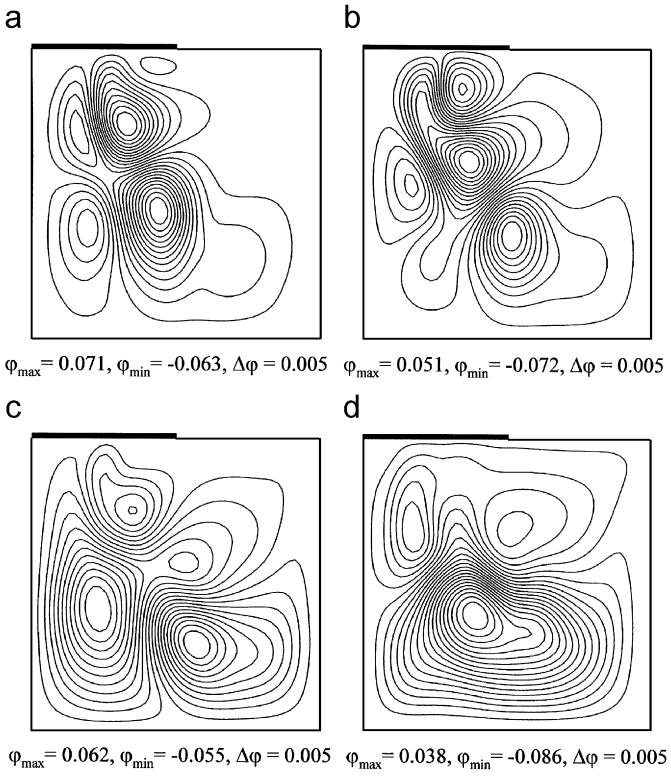


Fig. 8. Streamlines for the first four basic modes obtained by POD from the purely buoyancy-driven oscillatory flow at ($Gr = 2.52 \times 10^7$, $Ma = 0$), (a) mode 1, 22.1%; (b) mode 2, 19.5%; (c) mode 3, 13.4%; and (d) mode 4, 9.9%.

guessed in the above section. This is illustrated by the first four basic modes for the oscillatory flow at ($Gr = 2.52 \times 10^7$, $Ma = 4.94 \times 10^3$) which are shown in Fig. 9. The characteristic structures of these basic modes are clearly similar to those of the purely buoyancy-driven oscillatory flow (see Fig. 8), except that modes 3 and 4 have permuted.

With the further increase of *Ma,* the Marangoni instability is eventually triggered. At ($Gr = 2.52 \times 10^7$, $Ma = 4.94 \times 10^4$), as shown in Fig. 10 through the first four basic modes, the characteristics of the Marangoni instability appear in the basic modes, but this instability is not plainly dominant. Indeed, the first two modes clearly come from the Marangoni instability with a contribution of 46.6% to the fluctuation kinetic energy, whereas the third and fourth modes come from the buoyancy instability with a contribution of 40.2%, a contribution only slightly smaller than the Marangoni instability contribution. But for larger values of *Ma* ($Ma \geqslant 4.94 \times 10^5$), the Marangoni instability becomes clearly dominant. Fig. 11 shows the first two basic modes for the case at ($Gr = 2.52 \times 10^7$, $Ma = 4.94 \times 10^5$). These first two modes inherit the main characteristics of the Marangoni instability and capture most of the fluctuation kinetic energy (about 98%). As mentioned in the previous section, the conclusions for these two cases can not be clearly inferred from a pure DNS analysis with comparisons of the instantaneous DNS flow fields (as those shown in Fig. 3). This still confirms that the POD can be a useful tool to analyze the instabilities in complicated situations as the Cz crystal growth.

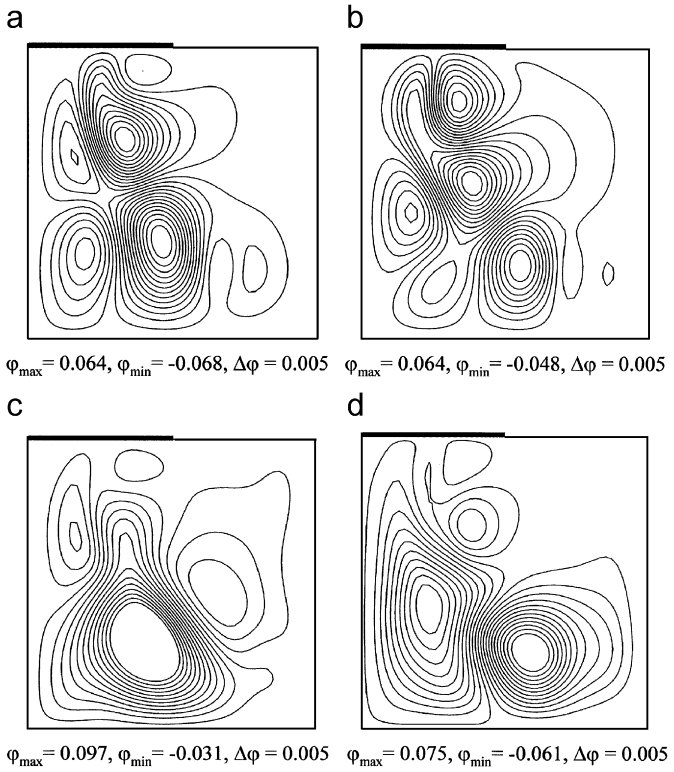


Fig. 9. Streamlines for the first four basic modes obtained by POD from the buoyancy- and Marangoni-driven oscillatory flow at ($Gr = 2.52 \times 10^7$, $Ma = 4.94 \times 10^3$), (a) mode 1, 19.1%; (b) mode 2, 15.3%; (c) mode 3, 14.6%; and (d) mode 4, 13.8%.

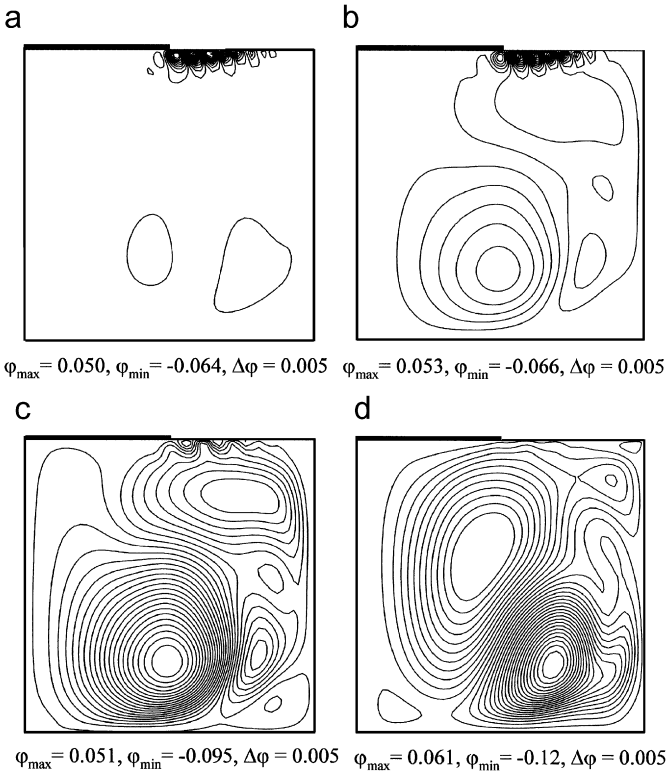


Fig. 10. Streamlines for the first four basic modes obtained by POD from the buoyancy- and Marangoni-driven oscillatory flow at ($Gr = 2.52 \times 10^7$, $Ma = 4.94 \times 10^4$), (a) mode 1, 23.5%; (b) mode 2, 23.1%; (c) mode 3, 22.4%; and (d) mode 4, 17.8%.

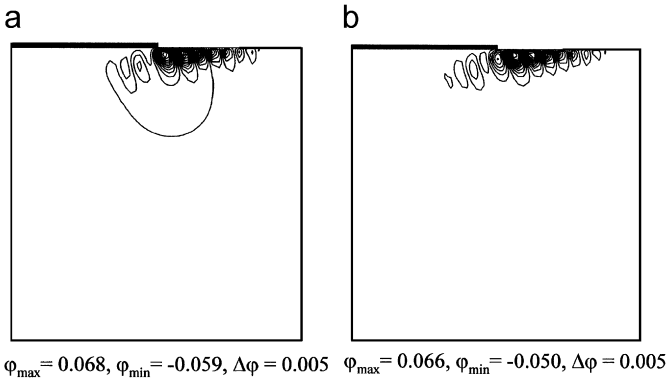


Fig. 11. Streamlines for the first four basic modes obtained by POD from the buoyancy- and Marangoni-driven oscillatory flow at ($Gr = 2.52 \times 10^7$, $Ma = 4.94 \times 10^5$), (a) mode 1, 50.6%; and (b) mode 2, 47.5%.

### 5.3. Behavior of the main modes triggering the instabilities

We want to give some further comments on the main modes involved in this study, i.e. those responsible for the buoyancy instability (Fig. 4) and those responsible for

the Marangoni instability (Fig. 5). The objective is to see what features these main modes give to the instability they trigger.

Concerning the buoyancy instability, most of the fluctuating kinetic energy (93%) is carried by the first two modes, but the first mode is really dominant with about 60% of this energy. The oscillatory behavior in this case may therefore be well reproduced by taking into account the contribution of this first mode alone. According to Eqs. (10) and (15), the streamfunction $\varphi(\boldsymbol{x},\tau)$ can be expressed in terms of the $M$ main modes as $\varphi(\boldsymbol{x},\tau)=\bar{\varphi}(\boldsymbol{x})+\sum_{i=1}^{M}a_i(\tau)\phi_i(\boldsymbol{x})$, where $\bar{\varphi}(\boldsymbol{x})$ and $\phi_i(\boldsymbol{x})$ are the streamfunctions of the mean field, $\bar{V}(\boldsymbol{x})$, and the $i$th mode, $\boldsymbol{\Phi}_i(\boldsymbol{x})$, respectively, and $a_i(\tau)$ describes the temporal contribution of $\boldsymbol{\Phi}_i(\boldsymbol{x})$. For the case considered here, $a_i(\tau)$ is shown in Fig. 12a for $i=1,2$, $\bar{\varphi}(\boldsymbol{x})$ in Fig. 12b, and $\phi_1(\boldsymbol{x})$ in Fig. 4a. If we only consider the first mode in the expansion ($M=1$), the streamfunction is given by $\varphi(\boldsymbol{x},\tau)=\bar{\varphi}(\boldsymbol{x})+a_1(\tau)\phi_1(\boldsymbol{x})$. The instantaneous streamlines thus obtained at two instants indicated by A and B in Fig. 12a are shown in Figs. 12c and d. Points A and B correspond to the positive and negative extreme values of $a_1(\tau)$, respectively. It is clear that Figs. 12c and d look similar to Figs. 3a and b obtained by DNS, which indicates that the first mode is actually the main contributor to the modifications of the instantaneous streamlines observed in Figs. 3a and b. In this first POD mode (Fig. 4a), the main feature is the intense and large roll located in the bottom-left corner of the geometry, i.e., close to the axis of the Cz crucible. When this roll turns in the same direction as the mean flow, i.e., anticlockwise (positive values of $a_1(\tau)$), it reinforces the flow in the bottom-left corner as observed in Fig. 3a. Then, when this roll turns clockwise (negative values of $a_1(\tau)$), it decreases the intensity of the flow and modifies the streamlines orientation in this bottom-left corner as observed in Fig. 3b. The analysis therefore shows that the oscillatory behavior driven by the buoyancy

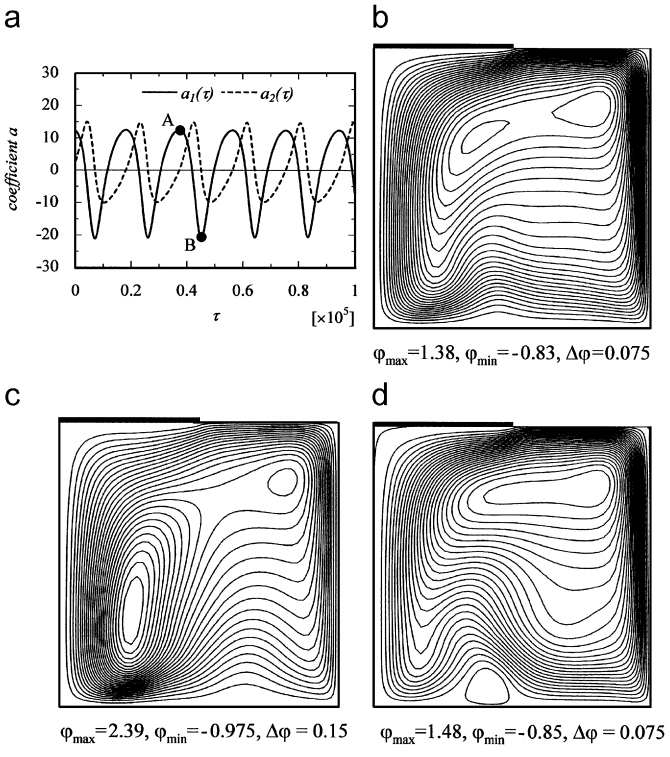


Fig. 12. Time variation of the coefficient $a_1$ and $a_2$ (a), streamlines for the mean flow (b), and instantaneous streamlines for the reconstructed flow taking into account the contribution of the first mode alone (at instant A (c) and at instant B (d)) for the buoyancy instability at ($Gr=5.04\times10^6$, $Ma=0$).

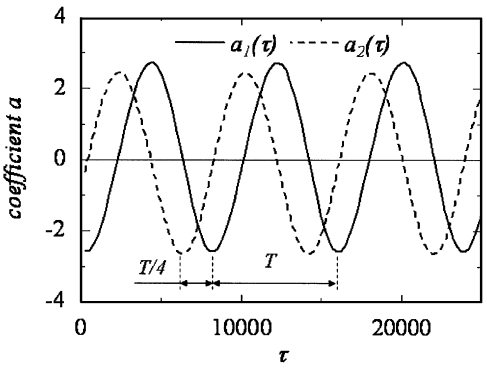


Fig. 13. Time variations of coefficient $a_1$ and $a_2$ for the Marangoni instability at ($Gr=0$, $Ma=4.94\times10^4$).

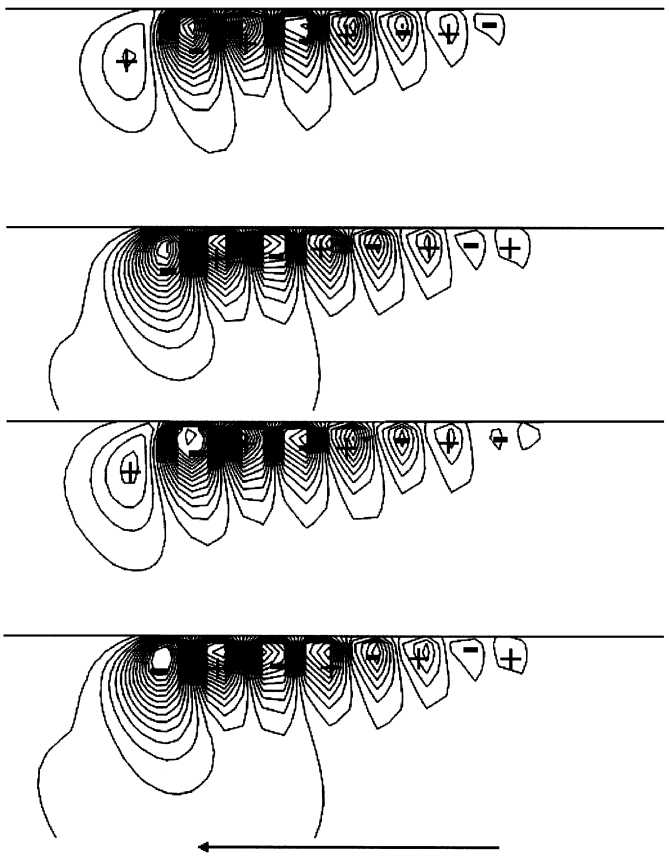

Fig. 14. Instantaneous streamlines obtained at four different instants from the streamfunction $\varphi(\boldsymbol{x},\tau)=a_1(\tau)\phi_1(\boldsymbol{x})+a_2(\tau)\phi_2(\boldsymbol{x})$ for the Marangoni instability at ($Gr=0$, $Ma=4.94\times10^4$). '+' and '−' denote the rotation direction of roll.

instability corresponds to a standing wave connected to the rotation of the main roll of the first mode alternatively in anticlockwise and clockwise directions.

Concerning the Marangoni instability, the first two modes which capture most of the fluctuating kinetic energy (more than 99%) have similar contributions. The spatial structure of these two modes (Figs. 5a and b) is similar and corresponds to multi-rolls appearing near the upper free surface. These rolls are created in the zone of high horizontal velocity (and high shear) due to the Marangoni effect, and their size increases from right to left, in the direction of the flow. Considering Figs. 5a and b more attentively, we can see that a spatial shift of half a roll (equivalent to a quarter of wavelength) exists between the two modes. Moreover, the time variations $a_1(\tau)$ and $a_2(\tau)$ associated to these modes (Fig. 13) have the same period $T$, but the corresponding signals are shifted by $T/4$. Such combination of spatial and temporal shifts is typical of a traveling wave structure. This is illustrated in Fig. 14, where is shown a zoom on the instantaneous streamlines obtained at four different instants from the streamfunction $\varphi(\boldsymbol{x},\tau) = a_1(\tau)\phi_1(\boldsymbol{x}) + a_2(\tau)\phi_2(\boldsymbol{x})$. A traveling wave structure moving from the right to the left, i.e. in the direction of the flow, is clearly depicted in this figure. This traveling wave structure seems to be a characteristic feature of the Marangoni instability in our study.

## 6. Conclusion

Proper orthogonal decomposition (POD) was traditionally used to disclose the basic structures of complicated flows or to reproduce real-time evolutions with a restricted number of chosen modes. In this paper, an attempt at applying POD to analyze the instability of oscillatory flows driven by several instabilities was conducted. Axisymmetric Czochralski melt flows involving both buoyancy and surface tension were used to demonstrate the potentiality of POD in such a domain. Numerical simulations were performed to obtain the oscillatory flow fields at various sets of the Grashof and the Marangoni numbers. POD was then used to extract the basic modes. By comparing the basic modes of the flow driven by both buoyancy and surface tension with those of the flow driven by a single effect, the instability responsible for the oscillatory flow was revealed. In addition, the proposed approach can indicate the characteristic spatial structures of instabilities, for example, the basic modes residing in the buoyancy-induced instability are global and rotating, and those in the Marangoni-induced instability are localized near the free surface and traveling. The results suggest that POD could really be a powerful method of instability analysis. But more application examples and quantitative analyses are further required to really assess the potentiality of the method.

## Acknowledgment

Project 50576079 supported by NSFC.

## References

[1] D.T.J. Hurle, J. Crystal Growth 65 (1983) 124.
[2] C.J. Jing, N. Imaishi, S. Yasuhiro, Y. Miyazawa, J. Crystal Growth 200 (1999) 204.
[3] C.J. Jing, N. Imaishi, S. Yasuhiro, Y. Miyazawa, J. Crystal Growth 216 (2000) 372.
[4] C.J. Jing, N. Imaishi, S. Yasuhiro, Y. Miyazawa, Int. J. Heat Mass Trans. 43 (2000) 4347.
[5] C.J. Jing, M. Kobayashi, T. Tsukada, M. Hozawa, T. Fukuda, N. Imaishi, K. Shimamura, N. Ichinose, J. Crystal Growth 252 (2003) 550.
[6] C.J. Jing, A. Hayashi, M. Kobayashi, T. Tsukada, M. Hozawa, N. Imaishi, K. Shimamura, N. Ichinose, J. Crystal Growth 259 (2003) 367.
[7] D.C. Miller, T.L. Pernell, J. Crystal Growth 53 (1981) 523.
[8] D.C. Miller, T.L. Pernell, J. Crystal Growth 57 (1982) 253.
[9] K. Shigematsu, Y. Anzai, S. Morita, M. Yamada, H. Yokoyama, Jpn. J. Appl. Phys. 26 (1987) 1988.
[10] S. Morita, H. Sekiwa, H. Toshima, Y. Miyazawa, J. Ceram. Soc. Japan 101 (1993) 108.
[11] A.D.W. Jones, J. Crystal Growth 61 (1983) 235.
[12] A.D.W. Jones, Progr. Cryst. Growth Charact. 9 (1984) 165.
[13] A.D.W. Jones, J. Crystal Growth 69 (1984) 165.
[14] A.D.W. Jones, J. Crystal Growth 94 (1989) 421.
[15] S. Enger, B. Basu, M. Breuer, F. Durst, J. Crystal Growth 219 (2000) 144.
[16] C.J. Jing, T. Tsukada, M. Hozawa, K. Shimamura, N. Ichinose, J. Crystal Growth 256 (2004) 505.
[17] J.L. Lumley, in: A.M. Yaglom, V.I. Tatarski (Eds.), Atmospheric Turbulence and Radio Wave Propagation, Nauka, Moskow, 1967, p. 166.
[18] L. Sirovich, Quart. Appl. Math. XLV (1987) 561.
[19] L. Sirovich, H. Park, Part I. Theory, Part II. Numer. Results, Phys. Fluids A 2 (1990) 1649.
[20] H. Gunes, Fluid Dyn. Res. 30 (2002) 1.
[21] C.J. Jing, D. Henry, H. Ben Hadid, N. Imaishi, Phys. Fluid 15 (2003) 2152.
[22] T. Suzuki, H. Kawamura, Trans. JSME 60 #578 (B) (1994) 58 (in Japanese).
[23] H.M. Park, D.H. Cho, Int. J. Heat Mass Transfer 39 (1996) 3311.